PHYSICAL REVIEW FLUIDS **6**, 013701 (2021)

Editors' Suggestion

Electrosprays of highly conducting liquids: A study of droplet and ion emission based on retarding potential and time-of-flight spectrometry

Manuel Gamero-Castaño [*] and Albert Cisquella-Serra
Department of Mechanical and Aerospace Engineering, University of California,
Irvine, California 92697, USA

(Received 29 September 2020; accepted 8 December 2020;
published 14 January 2021)

Electrosprays of highly conducting liquids operated in the cone-jet mode produce charged nanodroplets of controllable size and molecular ions. The study of this electrospraying regime is challenging due to the lack of experimental techniques for probing these nanometric systems, and the higher complexity of the physics associated with the onset of ion field emission and self-heating. Jet parameters in the breakup region such as its radius, velocity, potential, and electrification level are key for understanding the formation of droplets and emission of ions, and useful to validate numerical models of cone jets. In the case of micron-sized jets, these quantities can be determined with the values of the retarding potentials and mass-to-charge ratios of the droplets produced by the breakup. This article uses this technique to investigate the parameters of nanometric jets. Retarding potential and mass-to-charge distributions of the beam are measured with retarding potential and time-of-flight analyzers operated in tandem. This combination makes it possible to differentiate between droplets of similar mass-to-charge ratios which, unlike in the case of micrometric jets, are needed to apply the technique. Aside from the jet parameters, the experimental characterization also reveals with great detail the composition of the beam, which includes primary ions emitted from the jet breakup; ions resulting from the desolvation of primary ions; stable primary droplets produced at the breakup; smaller droplets resulting from the Coulomb explosion of unstable primary droplets; and small primary droplets that evaporate a significant fraction of their charge in flight. An analysis of the breakup, parametrized by dimensionless numbers, explains this complexity. Although the experimental characterization only studies the electrosprays of the ionic liquid 1-ethyl-3-methylimidazolium bis(trifluoromethylsulfonyl) imide, the analysis is general and can be used to understand the beams of other highly conducting liquids.

DOI: 10.1103/PhysRevFluids.6.013701

I. INTRODUCTION

The electrospraying technique operated in cone-jet mode makes it possible to atomize a liquid into sprays of charged droplets of controllable average diameter from a feeding channel that can be orders of magnitude larger than the droplets [1,2]. A liquid is typically fed to a pointed emitter, where the interaction between an imposed electric field, free charge, surface tension, and flow dynamics drive the liquid into a conical shape known as Taylor cone, from whose tip a slender and steady jet forms. The jet has a significant amount of net charge concentrated on its surface and is accelerated by the force of the electric field acting on it, which reduces the diameter of the jet

---

[*] mgameroc@uci.edu

©2021 American Physical Society

as the fluid moves downstream [3]. The stabilizing effect of the acceleration dies out sufficiently downstream, and the jet breaks into droplets due to capillary instability [4]. An ideal Taylor cone exhibits a singularity on the electric field and capillary pressure at its vertex, while the physical system has a correspondingly small transition region between cone and jet, with very large fields. As long as the imposed electrification is sufficiently high to maintain the sharpness of the meniscus tip, the physics in this small region is largely decoupled from far fields and fully determines the properties of the transition region and its jet [5,6]. Thus, in this electrospraying mode, local properties of the transition region (e.g., surface profile, surface charge density, flow field) as well as global observables fixed in the transition region such as the electrospray current, only depend on the physical properties of the liquid and its flow rate, and are largely independent of the potential and geometry of the emitter.

The technological applications of an atomization technique that enables the practitioner to fine tune the diameter of droplets down to a few nanometers are numerous, and has motivated fundamental research aimed at both the experimental characterization and modeling of cone jets [7–9]. Cone jets of highly conducting liquids (electrical conductivities of the order or larger than 0.5 S/m), needed to produce nanodroplets and nanojets, are an operational limit for which detailed knowledge is still lacking. Several reasons have contributed to this: (a) the experimental characterization of most electrospray variables in this limit is challenging due to the reduced dimensions of the jet and droplets (e.g., optical techniques for measuring droplet sizes and jet shapes are not applicable); and (b) processes such as ion field emission and self-heating due to Ohmic and viscous dissipation, which are irrelevant at lower conductivities, become now important making the modeling more difficult and the experimental phenomenology more complicated [10–12]. The goal of this article is to improve the understanding of cone jets of highly conducting fluids through the determination and analysis of jet parameters such as the velocity and potential at the breakup, and its Ohnesorge and Taylor numbers. This information is important to understand the physics of the cone jet and breakup, and to validate numerical models [6,13,14]. We obtain these parameters from the distributions of charged droplets and ions in the beams, measured with retarding potential and time-of-flight spectrometers. The article focuses on the characterization of the ionic liquid 1-ethyl-3-methylimidazolium bis(trifluoromethylsulfonyl) imide (EMI-Im [15]) due to our interest in this liquid for electrospray propulsion [16]. However, the analysis is done in terms of dimensionless numbers defining the state of the cone jet, and the findings and results for EMI-Im are applicable to other liquids operating in the high-conductivity regime.

II. EXPERIMENTAL SETUP

Figure 1 is a sketch of the experimental setup. The electrospray source is operated inside a vacuum chamber, needed to characterize its beams with time-of-flight and retarding potential analyzers [17]. The emitter is the chamfered and metallized end of a fused silica tube with an outer diameter of 360 μm, an inner diameter of 40 μm, and a length of 0.688 m. The opposite end exits the chamber through a vacuum fitting, and is submerged in a vial with EMI-Im placed at the bottom of a hermetic glass bottle. Surrounding the vial there is a bed of Drierite desiccant for eliminating water vapor molecules that could be absorbed by the hydrophilic EMI-Im (the vial with the liquid is open to the atmosphere of the hermetic bottle). A cylinder with pressurized argon, a mechanical pump, a pressure gauge, and a manifold with a system of valves are used to control the pressure in the bottle and feed the desired amount of EMI-Im to the emitter. The hydraulic resistance of the fused silica line was calibrated with a bubble flow meter, which confirmed the validity of using the Poiseuille law with the nominal length and inner radius of the line to determine the liquid flow rate Q from the applied pressure. During operation, a roughing mechanical pump and a turbomolecular pump bring the pressure in the vacuum chamber down to 2×10^{-6} Torr.

The liquid is electrosprayed into charged droplets and ions by setting a voltage difference ϕ_E between the emitter and an extractor electrode. All data reported in this article were taken at $\phi_E = 1690$ V. The extractor is connected to the laboratory ground. The charged particles are accel-

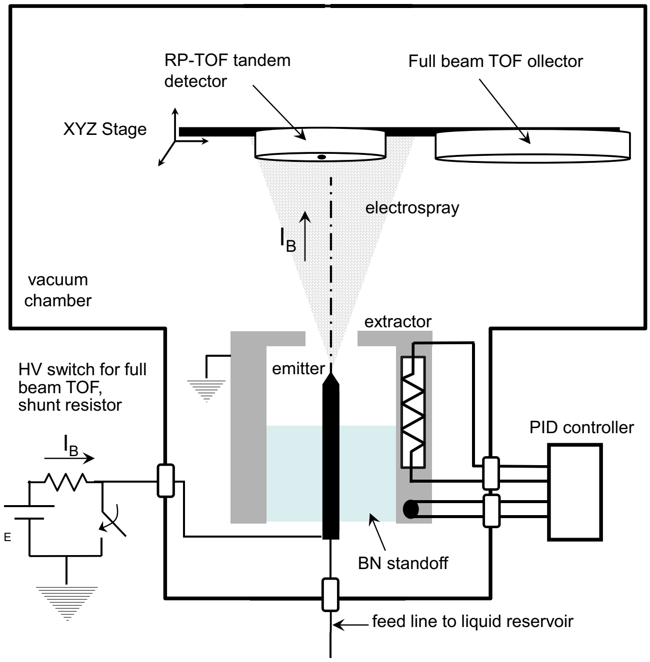

FIG. 1. Experimental setup: electrospray source, vacuum chamber, and detectors.

erated towards the extractor by the electric field, exit this inner region through an orifice perforated in the extractor and concentric with the emitter, and enter the outer, field-free region where they are analyzed. The temperature of the electrospray source is controlled below and above room temperature with the help of an electric heater, a thermoelectric cooler (peltier), and a thermocouple, all mounted on the extractor and connected to a PID controller. Heat is readily transferred between the emitter and extractor through a cylindrical standoff of boron nitride, a material with good thermal conduction and electrical isolation properties, and which can be mechanized to provide the required axial alignment between the emitter tube and the extractor. The current I_B emitted by the electrospray is measured in the high-voltage line powering the emitter, using a shunt resistor and an isolation amplifier for transferring this small voltage signal to laboratory ground. The full beam is characterized with a time-of-flight (TOF) setup that measures the beam current striking a large collector with an electrometer, and uses a high-voltage switch for rapidly shorting the electrospray source to ground [18]. The mapping between mass-to-charge ratio ζ and time of flight τ_{TOF}

$$\zeta = 2\phi_{\mathrm{RP}}\left(\frac{\tau_{\mathrm{TOF}}}{L_{\mathrm{TOF}}}\right)^2 \tag{1}$$

provided by this detector is approximate due to two experimental uncertainties: the collector is a plane perpendicular to the beam axis and the length L_{TOF} traveled by a particle varies along the surface of the collector; and the particles have a distribution of retarding potentials ϕ_{RP}. The retarding potential of a charged particle, defined as the sum of its kinetic and potential energy divided by the charge

$$\phi_{\mathrm{RP}} = \tfrac{1}{2}\zeta v^2(\mathbf{x}) + \phi(\mathbf{x}), \tag{2}$$

is a constant of motion in an electrostatic field. When an approximate $\zeta(\tau_{\mathrm{TOF}})$ mapping is needed from the signal of this instrument, for example to estimate the mass-to-charge ratio distribution of the whole beam, its thrust or mass flow rate [18], we use (1) with the distance between the extractor and collector at the axis, and the average value of the retarding potential.

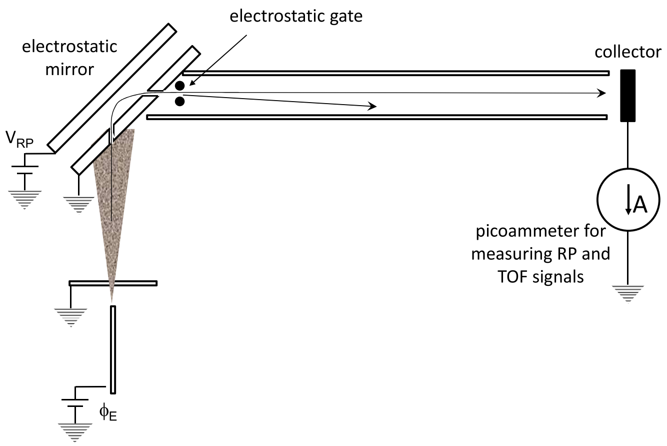

FIG. 2. Retarding potential (electrostatic mirror) and time-of-flight analyzers operated in tandem.

The retarding potential and time-of-flight analyzers in Fig. 2, operated in tandem, eliminate these two uncertainties. The mirror, with a voltage difference V_{RP} between plates, filters the incoming particles by retarding potential and only those with $\phi_{\mathrm{RP}} = V_{\mathrm{RP}}$ are transferred through [19]. The distance between the entry and exit orifices, the gap between the plates, the plate thickness, and the diameter of the orifices are 5.08 cm, 2.54 cm, 0.95 cm, and 1.58 mm, respectively. The current of the particles exiting the mirror and striking a small collector is measured with a fast electrometer. The collector is 15.6 cm downstream from an electrostatic gate placed at the exit of the mirror. When the electrostatic gate is off and V_{RP} is swept the electrometer yields the retarding potential density distribution $dI/d(\phi_{\mathrm{RP}})$. On the other hand, when the gate is rapidly turned on at fixed V_{RP} to deflect the beamlet, the electrometer yields the time-of-flight distribution across the drift tube. With both ϕ_{RP} and L_{TOF} precisely known, this instrument provides an accurate mass-to-charge distribution.

The relevant physical properties of EMI-Im are its electrical conductivity K, viscosity μ, density ρ, surface tension γ, and dielectric constant ε. We investigate the electrosprays at two emitter temperatures: 21 °C and 50 °C. In this range only the conductivity and viscosity vary significantly. For reference, we use the following values for the physical properties [15,20]: $\rho = 1520$ kg/m^3, $\gamma = 0.0349$ N/m, $\varepsilon = 12.2$; $K(21\,^\circ\mathrm{C}) = 0.74$ S/m, $K(50\,^\circ\mathrm{C}) = 1.56$ S/m; and $\mu(21\,^\circ\mathrm{C}) = 0.032$ Pa/s, $\mu(50\,^\circ\mathrm{C}) = 0.012$ Pa/s.

III. EXPERIMENTAL CHARACTERIZATION OF ELECTROSPRAY BEAMS

A. Ion and droplet populations

Cone jets of fluids with low and moderate conductivities ($K \lesssim 0.1$ S/m) produce sprays of charged droplets. At higher conductivities, the electric field on the surface of the jet and droplets reaches values that induce ion emission, and the sprays contain both charged droplets and molecular ions [10]. EMI-Im operates in this dual droplet–ion emission regime. Figure 3 shows time-of-flight curves of full beams for several electrospray currents, at both 21 °C and 50 °C emitter temperature. In each measurement the electrospray is initially operated steadily and turned off at $\tau_{\mathrm{TOF}} = 0$, so that the current reaching the collector goes down to zero during a period reflecting the variation of times of flight of the particles in the beam. The derivative of this curve thus yields the distribution density function $dI_B/d\tau_{\mathrm{TOF}}$ of the full beam. All beams in Fig. 3 are formed by two families of particles, fast molecular ions and slower charged droplets. The fraction of the current emitted as ions is significant. The flux of ions j_{IFE} emitted from the surface is expected to follow Iribarne-Thomson's

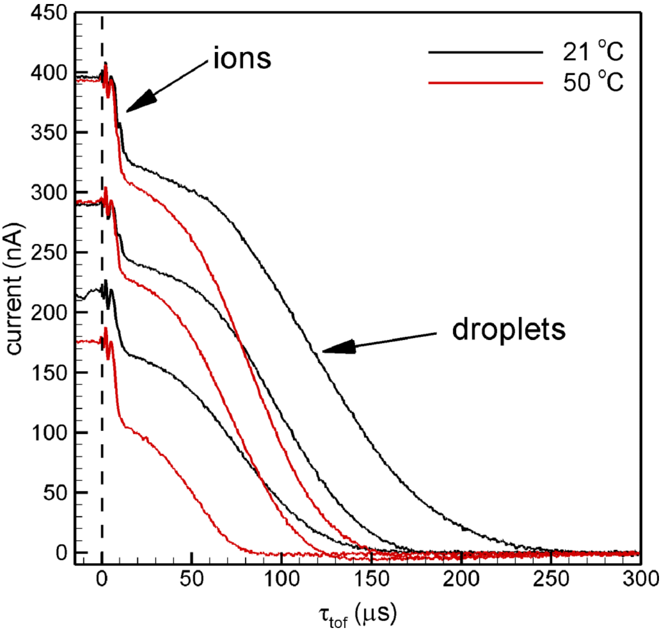

FIG. 3. Time-of-flight curves of the whole beam, for several beam currents and two emitter temperatures.

kinetic law [21]

$$j_{\mathrm{IFE}} = \frac{k_B T}{h} n \exp\left(-\frac{\Delta G_S^0 - G_E}{k_B T}\right),$$

$$\text{with } G_E = (e^3 E/4\pi\varepsilon_0)^{1/2}. \tag{3}$$

k_B, h, e, and ε_0 are the Boltzmann and Planck constants, the elementary charge, and the permittivity of the vacuum. T stands for the temperature, and E for the normal component of the electric field on the surface, on the vacuum side. ΔG_S^0 is the ion solvation energy and n the ion surface density. At fixed emitter temperature the ion fraction is a weak function of the flow rate, in agreement with the scaling of the electric field on the surface of the cone jet, $E_n^o \propto (\rho^{1/6}\gamma^{1/3}K^{1/3}/\varepsilon_o^{5/6})$, which does not depend on Q [14,22]. The ion current increases with the temperature of the emitter, as expected for this kinetic law. The average mass-to-charge ratio of the droplets emitted by cone jets scales as $\zeta \propto \rho I_B/\sqrt{\gamma K}$ [3], a trend that the TOF spectra reproduce: the time of flight of droplets increases with beam current at constant emitter temperature, and decreases with increasing temperature at constant beam current (K increases with temperature). The time-of-flight distributions of the droplet population, and therefore their mass-to-charge ratio distributions, are broad, extending to the values of molecular ions. The ζ distributions of electrosprayed droplets for liquids with lower conductivities are much narrower [23], typically narrower than the diameter distributions [24].

The two TOF detectors are designed to study the slower droplet population and, although they can differentiate between the velocities of droplets and ions, they cannot resolve the masses of different molecular ions present in these beams. This diversity is observable in the retarding potential curves, and a simple analysis can be used to find the molecular masses and origins of these ions (some ions are emitted from the surface of the cone jet while others are produced by desolvation of EMI-Im molecules from ions in flight). The retarding potential distribution in Fig. 4 is for a beam current of 255 nA and an emitter temperature of 50 °C. The black trace shows the overall spectrum, while the smaller vertical scale of the red trace highlights ionic peaks. The overall spectrum displays a continuum of particles starting at retarding potentials $\phi_{\mathrm{RP}} \approx 1200$ V. Within this continuum, TOF

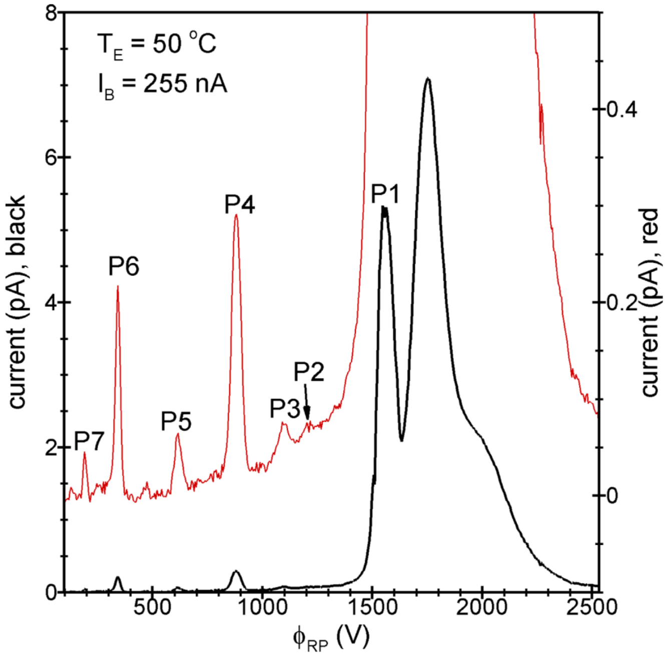

FIG. 4. Retarding potential curve illustrating multiple ionic peaks. Red and black traces are same spectra with different vertical scales.

analysis identifies the particles at $\phi_{\mathrm{RP}} \gtrsim 1650$ V as droplets, while the peak P_1 at $\phi_{\mathrm{RP}} \lesssim 1650$ and with a low-energy tail extending to 1200 V, is formed by ions. In addition to P_1, a series of isolated peaks P_2–P_7 can be distinguished from the background at smaller retarding potentials. The composition $A^+(AB)_{n-m}$ of these isolated peaks can be deduced under the assumption that they result from desolvation events

$$A^+(AB)_n \rightarrow A^+(AB)_{n-m} + m(AB) \tag{4}$$

happening to molecular ions $A^+(AB)_n$ from the P_1 peak, and taking place at ground potential upstream of the electrostatic mirror. A^+ stands for the EMI cation, and AB for the EMI-Im molecule. Since the desolvation of a molecule from an ion with a kinetic energy over 1000 eV insignificantly changes its velocity, it follows from (2) that the mass of the original ion divided by the mass of the desolvated ion must be equal to the ratio of their retarding potentials. Table I shows the retarding

TABLE I. Ionic peaks in Fig. 4. The comparison between the ratio of retarding potentials and masses indicate the composition of each ion.

Ion peak	ϕ_{RP} (V)	Composition	Transition	P_1/P_i ϕ_{RP} ratio	P_1/P_i mass ratio
P_1	1560	$A^+, A^+(AB), A^+(AB)_2, A^+(AB)_3\ldots$			
P_2	1212	$A^+(AB)_3$	$A^+(AB)_4 \rightarrow A^+(AB)_3 + AB$	1.29	1.30
P_3	1097	$A^+(AB)_2$	$A^+(AB)_3 \rightarrow A^+(AB)_2 + AB$	1.42	1.44
P_4	882	$A^+(AB)$	$A^+(AB)_2 \rightarrow A^+(AB) + AB$	1.77	1.78
P_5	616	$A^+(AB)$	$A^+(AB)_3 \rightarrow A^+(AB) + 2(AB)$	2.53	2.56
P_6	342	A^+	$A^+(AB) \rightarrow A^+ + AB$	4.56	4.52
P_7	190	A^+	$A^+(AB)_2 \rightarrow A^+ + 2(AB)$	8.22	8.05

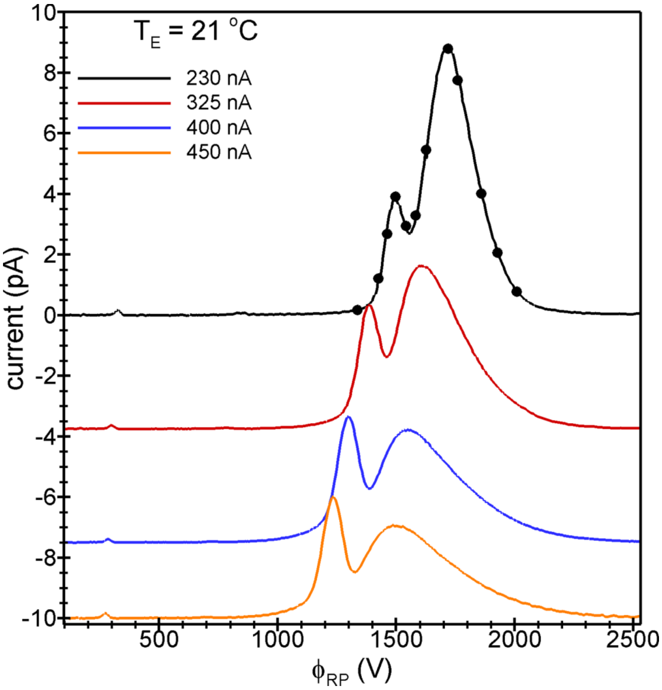

FIG. 5. Retarding potential distributions for several beam currents at 21 °C. Like in all experiments reported in this article the emitter potential is $\phi_E = 1690$ V.

potentials of each ionic peak, their inferred composition and desolvation reactions, the experimental ratios between the retarding potentials of P_1 and peaks P_2–P_7, and the ratios of the inferred masses. The ratio of the masses of the parent and desolvated ion, which always compares well with the ratio of the retarding potentials, confirms the composition assignments. We have observed that the intensities of desolvated ions increase with the background pressure, indicating that collisions with gas molecules can be a significant energy source enabling ion decomposition. However, these peaks still appear, although with lower intensities, at the regular working pressure of 2×10^{-6} Torr. Since the likelihood of such collisions along the ion path is extremely small at this pressure, it is possible that a fraction of the molecular ions emitted from the cone jet is unstable and spontaneously decomposes [25].

B. Tandem retarding potential and time-of-flight analysis

Figure 5 shows retarding potential curves for several beam currents. In all cases the emitter potential and temperature are $\phi_E = 1690$ V and 21 °C. All curves display a broad range of droplets, with a maximum and most of the area at retarding potentials smaller than ϕ_E and a tail extending above ϕ_E. The droplet region transitions into the sharper ionic peak P_1 in all cases. The desolvated ionic peaks are also present but barely visible in this vertical scale, except for the most intense P_6. In a related series of experiments in which the voltage difference between the emitter and extractor is kept at 1690 V while biasing the extractor with a positive potential V_B with respect to ground, the droplet and the P_1 regions (including the low-energy tail of P_1 but not the desolvated isolated peaks) translate with V_B while the retarding potential of the desolvated ionic peak P_i translates by the smaller amount $(\zeta_i/\zeta_1)V_B$. This agrees with the observation that the desolvated ions in P_2–P_7 originate at ground potential, and confirms that the particles in the droplet and P_1 regions are emitted in the region between the emitter and the extractor. The analysis in Sec. IV demonstrates that

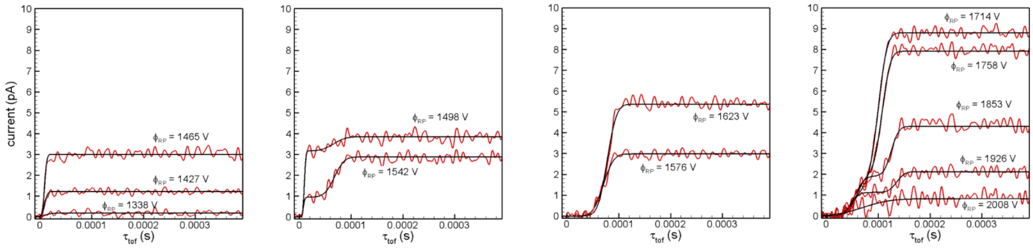

FIG. 6. Time-of-flight spectra at different retarding potentials (see black dots in Fig. 5) for $I_B = 230$ nA, 21 °C.

droplets and the ions around the maximum of P_1 are emitted from the jet's breakup region, while the ions in the low-energy tail of P_1 are likely evaporated from droplets in flight. The emission velocity of an ion evaporated from the cone jet is of the order of the fluid velocity, and therefore its kinetic energy at emission is negligible compared to that associated with its retarding potential $e\phi_{\mathrm{RP}}$. Therefore, the retarding potential of an ion in the P_1 region is a direct measure of the potential from which it evaporates. As the beam current increases the voltage difference $\phi_E - \phi_{\mathrm{RP}}(P_1)$ increases as well, indicating that the ion emission region moves downstream at increasing beam current. The fraction of droplets with retarding potentials larger than ϕ_E is at odds with the Ohmic and viscous dissipation of energy occurring in the cone jet [26]. These dissipation losses translate into a voltage deficit that lowers the retarding potential of the liquid in the jet below ϕ_E.

Figure 6 shows TOF spectra at several retarding potentials for the 230-nA beam (shown as black dots in Fig. 5 for reference). Each red trace is the average of 25 600 TOF measurements. The experimental curve is fitted to an error function (black trace) modeling a particle population, or to the sum of two error functions when there is evidence of two populations. The TOF spectra of the beamlets with retarding potentials of 1338, 1427, and 1465 V, i.e., within P_1 but at ϕ_{RP} lower than its maximum, have a single-particle family with very high velocities, readily identifiable as molecular ions (the average mass-to-charge ratio of these particles is 0.0134 g/C, i.e., 1295 u for a singly charged ion). The TOF curve at the maximum of P_1, $\phi_{\mathrm{RP}} = 1498$ V, contains mostly molecular ions and a second population of particles with $\langle\zeta\rangle = 0.587$ g/C. This second group of particles are charged droplets, with an estimated average radius of 11.8 nm. We use the maximum radius of a stable droplet, or Rayleigh limit

$$R_{\mathrm{Ray}}(\zeta) = \left(\frac{6\,\varepsilon_0^{1/2}\gamma^{1/2}}{\rho}\right)^{2/3}\zeta^{2/3}, \tag{5}$$

to estimate this radius [27]. At a retarding potential larger than 1498 V but still within P_1, $\phi_{\mathrm{RP}} =$ 1542 V, the TOF curve has the same two populations of ions and charged droplets, but the current of the droplets is now the larger fraction. The next two curves at 1576 and 1623 V, immediately after the local minimum in the retarding potential curve, have a single population of droplets with a relatively narrow distribution. The next spectrum, taken at the maximum of the retarding potential distribution $\phi_{\mathrm{RP}} = 1714$ V, is mostly formed by the same family of droplets, with the addition of a small fraction of droplets with lower mass-to-charge ratios. The spectra for the next three retarding potentials contain the same two droplet families, becoming more separated and having an increasing presence of the low-ζ population at increasing ϕ_{RP}. The last spectra at $\phi_{\mathrm{RP}} = 2008$ V are dominated by the low-ζ droplet population.

The phenomenology is similar for all beam currents at 21 °C: the retarding potential distribution has a region of droplets that extends several hundred volts on either side of the emitter potential, a joined region of ions P_1 at lower retarding potentials, and several isolated ion peaks at still lower retarding potential resulting from the desolvation of P_1 ions; there is a narrow overlap between the droplet region and P_1 where both ions and droplets coexist; there are two distinct groups of

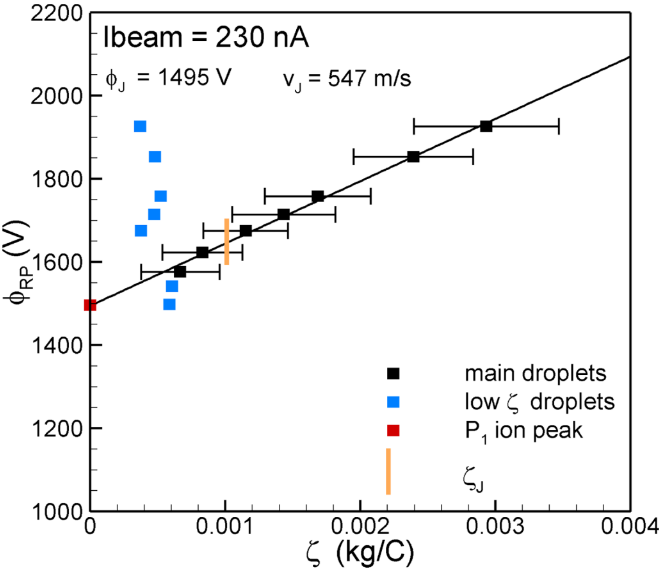

FIG. 7. Average mass-to-charge ratio vs retarding potential of droplet populations and ion peak P_1 from spectra in Fig. 12. Primary droplets and P_1 ions are emitted from the jet breakup.

droplets, one with higher mass-to-charge ratios distributed along a continuous range on either side of ϕ_E, and a second group with lower mass-to-charge ratios present in both the ion-droplet overlap and, mixed with the high-ζ droplet population, at retarding potentials near and above the maximum of the droplet distribution. In the latter case the current fraction of the low-ζ population increases with the retarding potential.

IV. ANALYSIS AND DISCUSSION

A. Determination of the velocity and potential of the jet in the breakup region

References [23,24] demonstrate a method for obtaining the nominal velocity and potential of the jet in the breakup region. The technique is based on the natural dispersion of the droplets' mass-to-charge ratio induced by the breakup, and assumes that the variations of potential and droplets' velocities in the unsteady breakup region are much smaller than the voltage drop along the cone jet and the velocity gained by the liquid along the jet. Under these conditions all droplets produced by the breakup are emitted at approximately the same nominal potential ϕ_J and velocity v_J. Thus, if the retarding potentials and mass-to-charge ratios of many i droplets emitted from the breakup region are available, ϕ_J and v_J can be obtained from the linear regression

$$\phi_{\mathrm{RP},i} = \tfrac{1}{2} v_J^2 \zeta_i + \phi_J. \tag{6}$$

This model is tested in Fig. 7 by plotting the average mass-to-charge ratio of the droplet distributions in Fig. 6 versus their retarding potentials. The droplets in the high-ζ population, with standard deviations given by the horizontal bars, follow (6) well, suggesting that they are indeed emitted from a region in which the variations of potentials and velocities are small. This common region for the majority of the droplets in the beam can only be the jet breakup. Henceforth, this population will be referred to as primary droplets. The y intercept and the slope of the linear fitting yield the nominal potential and velocity of the jet, $\phi_J = 1547$ V and $v_J = 547$ m/s. ϕ_J coincides with the retarding potential at the maximum of P_1, marked in the figure by a red point. Thus, the ions near the maximum of the P_1 peak are emitted from the breakup region as well. This explains the sharp transition between ions and droplets in the retarding potential curves: since the kinetic energy of

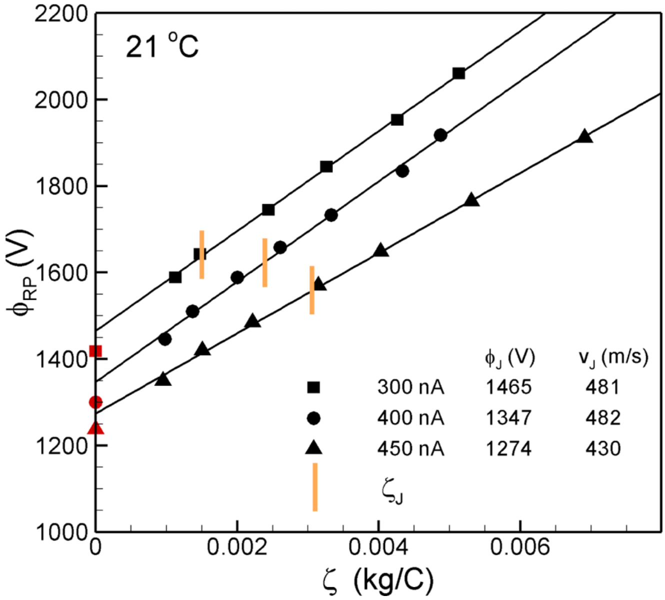

FIG. 8. Average mass-to-charge ratio vs retarding potential of primary droplets and ion peak P_1, for several beam currents at 21 °C.

an ion divided by its charge is insignificant compared to that of a droplet in the same emission region, the retarding potentials of the droplets must always be larger than the retarding potential of ions. On the other hand, the droplet population with low ζ does not conform to (6), suggesting that they are not emitted directly from the breakup region or, if they are, undergo processes that modify their retarding potentials or their mass-to-charge ratios. Coulomb explosions and ion emission from droplets in flight are mechanisms that may explain the anomalous $\phi_{\mathrm{RP}}(\zeta)$ relation, and Sec. IV C discusses this possibility. Figure 7 also shows the charge-to-mass ratio of the jet, $\zeta_J = \rho Q/I_B$, as an orange bar over the fitting. Most of the primary droplets have a mass-to-charge ratio higher than the jet. This large departure from conservation of mass and charge in the breakup, which requires $\langle\zeta_D\rangle \approxeq \zeta_J$, may be explained by the natural angular segregation of droplets by mass-to-charge ratio induced by the beam's space charge, which concentrates the droplets with higher ζ towards the axis [24]. However, the substantial presence of ions and low-ζ droplets in the same angular location suggests that other phenomena may contribute to the drastic disappearance of the large fraction of the primary droplets with $\zeta_D \lesssim \zeta_J$.

The normal component of the electric field along the cone jet, which is the key parameter driving ion emission, exhibits two local maxima [10,11]: one is located at the base of the jet where the dominant mechanism for charge transport transitions from bulk conduction to surface charge convection [14]; and a second maximum occurs in the breakup region, on those droplets (and probably at jet pinching points) where the curvature and electrification intensify. Since the retarding potential of the most energetic ions coincides with the potential at the jet breakup, and no ions with the higher retarding potentials indicative of emission from the transition region are detected, the local maximum of the electric field at the base of the jet must not be sufficiently high to evaporate ions in electrosprays of EMI-Im.

Figure 8 shows the linear regression for the primary droplets of the 300-, 400-, and 450-nA beams, at 21 °C. The linear model fits well the points, and the y intercepts are near the retarding potential of the maxima of the P_1 peaks. The low-ζ droplets are not shown to avoid crowding the chart, but their phenomenology is identical to that shown in Fig. 7. All beams studied at 21 °C display the same patterns of primary droplets and P_1 ions being emitted from the breakup region,

TABLE II. Relevant parameters of EMI-Im electrosprays at 21 °C: flow rate Q; beam current I_B; dimensionless flow rate $\tilde{Q}$ and beam current $\tilde{I}$; nominal mass-to-charge ratio ζ_J and velocity v_J of the jet in the breakup; nominal jet radius R_J, and value normalized with Gañán-Calvo's characteristic length $\tilde{R}_J$; Rayleigh limit radius $R_{\mathrm{Ray}}(\zeta_J)$ of droplet with mass-to-charge ratio ζ_J; potential drop along the cone jet $\phi_E - \phi_J$; normal electric field on the jet's surface $E^o_{n,J}$; jet's viscosity J and electrification Ψ parameters.

Q (nl/s)	I_B (nA)	$\tilde{Q}$	$\tilde{I}$	ζ_J (g/C)	v_J (m/s)	R_J (nm)	$\tilde{R}_J$	$R_{\mathrm{Ray}}(\zeta_J)$ (nm)	$\phi_E - \phi_J$ (V)	$E^o_{n,J}$ (V/nm)	J	Ψ
0.153	230.0	612.0	86.3	1.01	547.0	9.42	0.273	17.0	196.0	0.802	0.00057	1.54
0.233	265.0	933.0	99.5	1.33	531.0	11.8	0.277	20.5	242.0	0.76	0.000714	1.73
0.297	300.0	1190.0	113.0	1.5	481.0	14.0	0.292	22.2	274.0	0.8	0.000848	2.28
0.375	325.0	1500.0	122.0	1.75	462.0	16.1	0.297	24.6	304.0	0.786	0.000971	2.52
0.464	350.0	1860.0	131.0	2.01	501.0	17.2	0.285	26.9	331.0	0.731	0.00104	2.33
0.562	375.0	2250.0	141.0	2.28	503.0	18.9	0.285	29.2	354.0	0.711	0.00114	2.42
0.629	400.0	2520.0	150.0	2.39	482.0	20.4	0.291	30.2	392.0	0.732	0.00123	2.77
0.743	425.0	2980.0	160.0	2.66	448.0	23.0	0.302	32.4	449.0	0.742	0.00139	3.21
0.905	450.0	3630.0	169.0	3.06	431.0	25.9	0.308	35.6	455.0	0.726	0.00156	3.46

the reduced presence of primary droplets with $\zeta_D \lesssim \zeta_J$, and low-ζ droplets that do not follow the breakup equation (6). Table II lists the velocity of the jets at the breakup and the voltage drop along the cone jet, $\phi_E - \phi_J$, together with other jet parameters discussed in Secs. IV B and IV C. Reference [17] shows that the voltage drop along the cone jet is independent of ϕ_E. This work also reports values for $\phi_E - \phi_J$ and v_J for electrosprays of EMI-Im. The $\phi_E - \phi_J$ values agree well with those in Table II, but the jet velocities are substantially higher. Reference [17] does not employ RP-TOF in tandem, and can not use (6) to determine ϕ_J and v_J. Instead, it identifies the P_1 peaks as ions emitted from the breakup, and in the absence of better information estimates the jet velocity as $[2(\phi_E - \phi_J)/\zeta_J]^{1/2}$. This estimate neglects dissipation and the generation of surface in the jet, and as a result yields a larger velocity.

B. Self-heating effects and universal jet radii

Table II lists the flow rates and currents of the EMI-Im beams characterized at 21 °C. These quantities are also given in dimensionless form $\tilde{Q} = \rho K Q/(\gamma \varepsilon_0)$ and $\tilde{I} = I_B/(\varepsilon_0 \gamma^2/\rho)^{1/2}$, for easier comparison with the literature. The $\{\tilde{Q}, \tilde{I}\}$ points are well fitted by $\tilde{I} = 2.39\tilde{Q}^{1/2} + 28.4$, in agreement with the well-established scaling law $\tilde{I} \simeq \alpha \tilde{Q}^{1/2}$ except for the large positive y intercept of 28.4. The value $\alpha = 2.6$ is a good fit for measurements of a large group of liquids [8], while a numerical solution finds $\alpha = 2.5$ for a liquid of similar dielectric constant (tributyl phosphate, $\varepsilon = 8.91$) [14]. The large positive y intercept for EMI-Im is associated with significant self-heating due to Ohmic and viscous dissipation typical of fluids with high conductivities, which increases the conductivity of the fluid along the transition region of the cone jet. If corrected for this effect by using a conductivity averaged over the transition region, the values of $\tilde{Q}$ would be larger than in Table II, resulting in a reduction of the y intercept [12].

The dimensionless flow rates at which EMI-Im can be electrosprayed are very high compared to other liquids (see, for example, Fig. 7 in Ref. [8]). In our experiments we find that the minimum stable flow rate of EMI-Im at room temperature is $\tilde{Q}_{\mathrm{min}} \approxeq 460$. This is to be expected for cone jets of highly conducting liquids with an elevated viscosity, a condition that can be evaluated in terms of $\mathrm{Re_K} = [\rho \varepsilon_o \gamma^2/(\mu^3 K)]^{1/3}$, a dimensionless number frequently used in the literature of cone jets. Its value for EMI-Im at 21 °C is $\mathrm{Re_K} = 8.53 \times 10^{-3}$. Reference [28] shows that the minimum flow rate for tributyl phosphate, a fluid with similar dielectric constant but $\mathrm{Re_K}$ values at least one order of magnitude larger than EMI-Im, scales as $\tilde{Q}_{\mathrm{min}} \simeq 1.87\mathrm{Re_K}^{-1.1}$. This relation yields $\tilde{Q}_{\mathrm{min}} = 353$ for $\mathrm{Re_K} = 8.53 \times 10^{-3}$, a value similar to that of EMI-Im.

Table II also lists the nominal radius of the jet $R_J = [Q/(\pi\, v_J)]^{1/2}$ and its dimensionless form normalized with Gañán-Calvo's characteristic length $\tilde{R}_J = R_J/r_G$, $r_G = [\rho\varepsilon_o Q^3/(\gamma K)]^{1/6}$ [5,29]. Aside from the nanometric radii of these jets, the near constancy of $\tilde{R}_J$ for all flow rates is noteworthy: while Q changes by a factor of 5.92, $\tilde{R}_J$ changes by a factor of 1.13. References [14,26] show that the geometry of the transition region of the cone jet, when made dimensionless with r_G, remains nearly invariant to changes of the flow rate. The near constancy of the dimensionless jet radii in Table II, $\tilde{R}_J \simeq \beta = 0.29$, extends this result valid for the transition region to the jet's breakup, suggesting that the condition triggering the breakup is also driven by the physics and processes of the transition region.

C. Equipotential jet breakup, droplet radii, and the effects of Coulomb explosions and ion evaporation

The broad mass-to-charge ratio distributions of droplets, the failure of the low-ζ droplets to conform to the breakup condition (6), the perplexingly high retarding potentials of some low-ζ droplets, and the potential presence of Coulomb explosions and ion evaporation from droplets in flight are important topics. A detailed investigation of these problems requires accurate modeling of the breakup at typical jet conditions, a numerical effort that is beyond the scope of this article. Instead, the following discussion will provide a basic explanation of the observed phenomenology and may guide future analytical work.

At low flow rates $\tilde{Q} \lesssim \varepsilon$, the jet breakup produces droplets with narrow distributions of diameters and mass-to-charge ratios. At higher flow rates an additional class of droplets with smaller diameters and mass-to-charge ratios, referred to as satellites, appears. Numerical models and visualization of experiments show that satellite droplets form in the pinching region of primary droplets, where charge accumulates due to the higher curvature and electric field. This process is associated with the increasing nonlinearity of the breakup, triggered by a sufficiently high value of the Reynolds number. At still higher flow rates, the jet breakup transitions to a regime with significantly broader distributions, without a clear separation between primary and satellite droplets. The latter breakup regime has been associated with the onset of lateral oscillations, induced by the destabilizing effect of increasing electrification [4,23,24,26]. The dimensionless Taylor number

$$\Psi = \frac{\sigma^2 R_J}{\varepsilon_0 \gamma} \simeq \frac{\alpha^2\beta^3}{4}\tilde{Q}^{1/2}, \tag{7}$$

approximately twice the ratio between the electrostatic stress and the capillary pressure, is a measure of the electrification of the jet. The pressure in the fluid is negative for $\Psi > 2$, a condition happening at the Rayleigh limit of droplets (5) and in all jets in Table II, except for the two lowest currents. The large value of Ψ in EMI-Im jets is a direct consequence of the high flow rates needed to make the electrospray stable, and will also be typical of most highly conducting ionic liquids due to their low Re_K values and associated high $\tilde{Q}_\mathrm{min}$.

Linear instability analysis is a standard technique for determining the initial growth rate of axisymmetric perturbation modes prescribed on the jet's surface [30]. A perturbation with a positive growth rate makes the jet unstable, and the wavelength λ of the perturbation yields the radius of the associated droplet $R_D = (3\lambda R_J^2/4)^{1/3}$. The perturbation with maximum growth rate produces the most likely droplet, with critical radius R_D^*. For the simplest case of an uncharged and inviscid jet, the ratio between R_D^* and the radius of the jet is $R_D^*/R_J = 1.89$. This ratio changes when viscous effects and electrification are important, e.g., it is well known that viscosity has a stabilizing effect in the breakup, increasing R_D^*/R_J [30]. Reference [23] provides formulas for the growth rate as a function of λ/R_J, Ψ, and the dimensionless parameter J describing viscous effects

$$J = \frac{\rho\gamma R_J}{\mu^2} \simeq \beta\tilde{Q}^{1/2}\mathrm{Re}_\mathrm{K}^2, \tag{8}$$

for several electrification limiting hypotheses, namely, equipotential breakup, constant volumetric charge, and charge bounded to the surface. Note the correspondence between J and the more

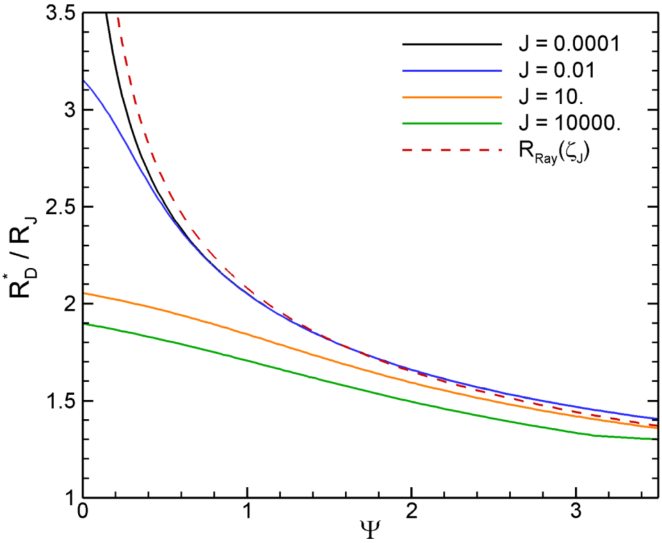

FIG. 9. Critical droplet radius R_D^* normalized with the radius of the jet, as a function of the Taylor Ψ and Ohnesorge numbers $\mathrm{Oh} = J^{-1/2}$; and Rayleigh limit of the droplet with the mass-to-charge ratio of the jet.

common Ohnesorge number $\mathrm{Oh} = J^{-1/2}$. The equipotential breakup is the appropriate scenario for EMI-Im jets due to the small ratio between the electrical relaxation time $t_r = \varepsilon\varepsilon_0/K$ and the characteristic flow time during the breakup. The latter can be estimated by balancing the always important capillary pressure with inertia $t_{\gamma\rho} = (\rho r_J^3/\gamma)^{1/2}$, or with the viscous stress $t_{\gamma\mu} = \mu r_J/\gamma$. The ratios of times for both cases are

$$\frac{t_r}{t_{\gamma\rho}} = \frac{\varepsilon}{\tilde{Q}^{3/4}}, \quad \frac{t_r}{t_{\gamma\mu}} = \frac{\varepsilon \mathrm{Re}_\mathrm{K}}{\tilde{Q}^{1/2}}. \tag{9}$$

In the case of EMI-Im, the very large values of the dimensionless flow rate and the low Re_K make the electrical relaxation time always much smaller than the characteristic flow time. Therefore, the surface charge must be near equilibrium throughout the breakup, shielding the fluid from external fields. For a equipotential breakup the initial growth rate $\sigma(x, J, \Psi)$ of a perturbation with wave number $x = 2\pi R_J/\lambda$, is found by eliminating y from [23]

$$\sigma \frac{\rho R_J^2}{\mu} = y^2 - x^2, \tag{10}$$

$$2x^2(x^2+y^2)\frac{\mathrm{I}_1'(x)}{\mathrm{I}_0(x)}\left[1 - \frac{2xy}{x^2+y^2}\frac{\mathrm{I}_1(x)\mathrm{I}_1'(y)}{\mathrm{I}_1'(x)\mathrm{I}_1(y)}\right] - (x^4 - y^4)$$
$$= J\left\{x(1-x^2)\frac{\mathrm{I}_1(x)}{\mathrm{I}_0(x)} - \Psi\frac{x\mathrm{I}_1(x)}{\mathrm{I}_0(x)}\left[1 + \frac{x\mathrm{K}_0'(x)}{\mathrm{K}_0(x)}\right]\right\}. \tag{11}$$

The wavelength $\lambda^*(J, \Psi)$ associated with the maximum growth rate yields the radius of the critical droplet

$$\frac{R_D^*(J,\Psi)}{R_J} = \left(\frac{3}{4}\frac{\lambda^*}{R_J}\right)^{1/3}. \tag{12}$$

Figure 9 shows R_D^*/R_J as a function of Ψ, for several values of J and an equipotential breakup. Note that for the case of inviscid breakup and marginal electrification, $J \to \infty$ and $\Psi \to 0$, R_D^*/R_J approaches the expected value of 1.89. Increasing values of the Taylor number make the critical droplet smaller, while strong viscous effects (decreasing J) make the critical droplet larger, especially when the importance of electrification is small. For the very large values of Ψ typical of EMI-Im jets the effect of J on the breakup is reduced, the destabilizing effect of electrification dominates over the stabilizing effect of viscosity, and R_D^*/R_J may fall substantially below 1.89. Note also that for moderate and highly electrified breakup R_D^*/R_J asymptotes fast to a single curve for sufficiently low values of J, with the curves for $J = 0.1$ and 0.0001 being nearly identical for $\Psi \gtrsim 0.5$. Clearly, the breakups of most highly conducting liquids are described by this asymptote.

The mass-to-charge ratio of the jet can be expressed in terms of Ψ:

$$\zeta_J = \frac{\rho}{2\varepsilon_0^{1/2}\gamma^{1/2}}\frac{R_J^{3/2}}{\Psi^{1/2}}, \tag{13}$$

which makes it possible to write the maximum stable radius of a droplet with mass-to-charge ratio ζ_J, given by the Rayleigh limit (5), as

$$\frac{R_{\mathrm{Ray}}(\zeta_J)}{R_J} = \frac{3^{2/3}}{\Psi^{1/3}}. \tag{14}$$

This relation is plotted in Fig. 9, and provides an interesting corollary: in an equipotential breakup with the very strong viscous and electrification effects typical of EMI-Im jets, the critical droplet charged with the mass-to-charge ratio of the jet is at, or very near, the Rayleigh limit. A droplet of critical radius with $\zeta_D < \zeta_J$ is unstable and should undergo a Coulomb explosion, while one with $\zeta_D > \zeta_J$ is stable; similarly, a droplet with $\zeta_D = \zeta_J$ is stable if its radius is smaller than R_D^*, and unstable otherwise. The dependence of the stability of a droplet on the ratios R_D/R_D^* and ζ_D/ζ_J is a consequence of the relative positions of the $R_D^*(J, \Psi)$ and $R_{\mathrm{Ray}}(\zeta_J)$ curves in Fig. 9.

To understand the effects of Coulomb explosions and ion emission in the observed populations of droplets, we next study the dependence between the radius and the mass-to-charge ratio of a droplet produced in an equipotential breakup $R_\phi(\zeta)$, and compare this function with the constraints associated with the Rayleigh instability limit $R_{\mathrm{Ray}}(\zeta)$, and the radius of the droplet $R_{\mathrm{IFE}}(\zeta)$ that would trigger ion field emission. The inherent randomness and nonlinearity of the breakup causes a variability in both the radii of the droplets, and in the mass-to-charge ratios of droplets for a given radius. However, the equipotential condition requires these two variables to be distributed in a band around the constraint

$$\phi_c \cong \frac{q_D}{4\pi\varepsilon_0 R_D} \longrightarrow \zeta_D \cong \frac{\rho}{3\varepsilon_0\phi_c}R_D^2, \tag{15}$$

where the characteristic potential ϕ_c can be approximated by the potential of the most likely droplet, i.e., that with the critical radius and mass-to-charge ratio ζ_J, $\phi_c = \rho R_D^{*2}/(3\varepsilon_0\zeta_J)$. Equation (15) does not take into account how neighboring droplets affect the potential of a given droplet, or conservation of charge; this would require solving numerically the long-deformation dynamics of the breakup, a complex problem beyond the scope of this article. In the actual breakup droplets with a given radius R_D are surrounded by droplets with different radii at different times, and therefore they will exhibit a distribution of mass-to-charge ratios; Eq. (15) is an approximation to the center of this distribution. After inserting the value of ϕ_c in (15), the sought relationship $R_\phi(\zeta)$ for the equipotential breakup is

$$\frac{R_\phi(\zeta)}{R_D^*} = \left(\frac{\zeta}{\zeta_J}\right)^{1/2}. \tag{16}$$

The dependence of the Rayleigh instability radius on the mass-to-charge of the droplet (5) can be recast in a similar form as

$$\frac{R_{\mathrm{Ray}}(\zeta)}{R_D^*} = \frac{R_{\mathrm{Ray}}(\zeta_J)}{R_D^*}\left(\frac{\zeta}{\zeta_J}\right)^{2/3}, \tag{17}$$

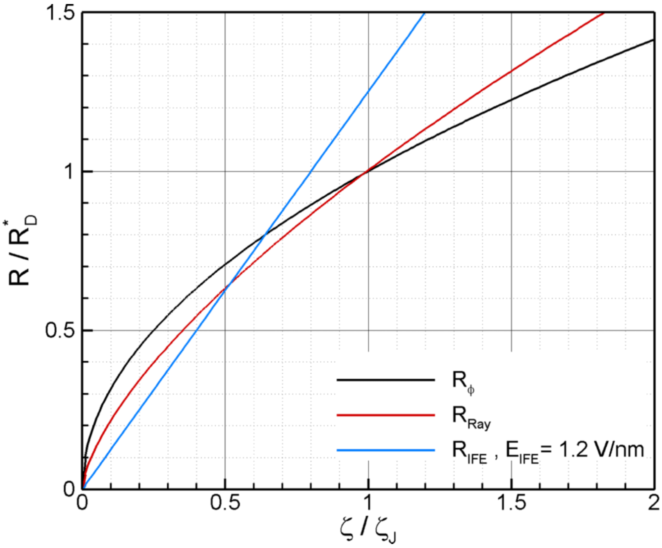

FIG. 10. Droplet radius normalized with the critical droplet radius $R_D^*(J,\Psi)$, for a beam current of 230 nA at 21 °C and three different mechanisms: equipotential breakup R_ϕ; Rayleigh limit R_{Ray}; and ion evaporation limit R_{IFE}, with $E_{\text{IFE}} = 1.2$ eV.

where $R_{\text{Ray}}(\zeta_J)/R_D^*$ is near one for EMI-Im, as illustrated by the ratio between functions (12) and (14) in Fig. 9. Finally, when the electric field on the droplet exceeds a critical value E_{IFE} promoting ion field emission, ions are emitted at constant droplet radius until the electric field is reduced just below E_{IFE}. A droplet with an electric field E_{IFE} on its surface exhibits the following dependency between its radius and mass-to-charge ratio, $R_{\text{IFE}}(\zeta)$:

$$E_n^o = \frac{q_D}{4\pi\varepsilon_0 R_D^2} \longrightarrow \frac{R_{\text{IFE}}(\zeta)}{R_D^*} = \frac{E_{\text{IFE}}}{E_D^*(\zeta_J)}\frac{\zeta}{\zeta_J}, \tag{18}$$

where $E_D^*(\zeta_J)$ is the electric field of the droplet of critical radius with mass-to-charge ratio ζ_J. Figure 10 plots (16), (17), and (18) with $E_{\text{IFE}} = 1.2$ eV, for the 230-nA beam; the plots for all other beam currents are similar due to the nearly coincidence between R_D^* and $R_{\text{Ray}}(\zeta_J)$ for all EMI-Im jets. The randomness of the breakup produces droplets with different mass-to-charge ratios, with average diameters given by (16). Droplets with $\zeta_D/\zeta_J > 0.98$ have radii smaller than their associated Rayleigh limit and are stable. Droplets with $0.64 < \zeta_D/\zeta_J < 0.98$ have diameters over the Rayleigh limit, are unstable, and break into fragments (probably one with the larger mass fraction, and higher ζ and ϕ_{RP} than the original droplet, and several smaller fragments with lower ζ and ϕ_{RP} than the original droplet). And droplets with $\zeta_D/\zeta_J < 0.64$ evaporate ions at constant radius, i.e., they trace horizontal paths starting on the curve $R_\phi(\zeta)$, in the direction of increasing ζ/ζ_J. Among these ion-evaporating droplets, the horizontal paths of those in the range $0.42 < \zeta_D/\zeta_J < 0.64$ intersect the ion evaporation line without crossing the Rayleigh limit. At this point, ion evaporation ceases, and because the radii are above the Rayleigh limit, the droplets are unstable and should explode. On the other hand, the horizontal paths of droplets with $\zeta_D/\zeta_J < 0.42$ cross the Rayleigh limit before intersecting the ion evaporation line, so that once the droplet stops shedding charge it has a stable radius. The variability of the mass-to-charge ratios of primary droplets, and therefore the domain accessible in Fig. 10, can be estimated as the maximum range covered by the horizontal bars in Fig. 7, $0.37 \leqslant \zeta/\zeta_J \leqslant 3.5$. The actual range is likely larger because we are only sampling droplets near the beam axis (we expect the smaller droplets with lower ζ to distribute preferentially away from the axis), and also because the mass-to-charge ratio of small primary droplets may not be detectable due to their expected transformation (Coulomb explosions and ion evaporation).

This analysis is consistent with the experimental observations: (a) an equipotential breakup, with its quadratic $\zeta_D(R_D)$ dependence, produces droplets with broad mass-to-charge ratio distributions, in agreement with the TOF spectra; (b) the experiments show that a large number of droplets produced at the breakup remain intact during flight. Most of these primary droplets have mass-to-charge ratios larger than ζ_J which, according to the analysis, favors droplet stability (these droplets do not reach the Rayleigh limit); (c) only a small fraction of the primary droplets reaching the collector have mass-to-charge ratios smaller than ζ_J. This absence suggests that most of the small primary droplets are unstable, transforming into other droplets that do not fulfill the breakup equation (6). Two new types of droplets with low mass-to-charge ratios are indeed observed in the beams (see blue squares in Fig. 7): one with the lowest retarding potentials among all droplets are likely fragments of Coulomb explosions; and one with retarding potentials spanning between the emitter potential and the largest retarding potentials among all droplets. The latter population is striking because despite its very low mass-to-charge ratios (it is the droplet population with lowest ζ), some of these droplets have the highest retarding potentials. We can only explain this population as being very small primary droplets produced at the breakup with an electrification level exceeding the ion evaporation limit (18), and which evaporate ions in flight at constant radius while being accelerated by a voltage drop $\Delta\phi_{EV}$. Using ζ_0 for the initial mass-to-charge ratio of the droplet at the breakup (its initial potential and velocity are ϕ_J and v_J), and ζ_f, ϕ_f, and v_f for the mass-to-charge ratio, potential and speed at the conclusion of ion evaporation ($\Delta\phi_{EV} = \phi_J - \phi_f > 0$), the retarding potential of the charge-depleted droplet is given by

$$\phi_{\mathrm{RP}} = \phi_f + \frac{1}{2}\zeta_f v_f^2 = \phi_f + \frac{1}{2}\zeta_f v_J^2 + \zeta_f \int_{\phi_f}^{\phi_J} \frac{d\phi}{\zeta}, \tag{19a}$$

$$\text{with} \quad \Delta\phi_{EV} < \zeta_f \int_{\phi_f}^{\phi_J} \frac{d\phi}{\zeta} < \frac{\zeta_f}{\zeta_0}\Delta\phi_{EV}.$$

The mass-to-charge ratio in the integrand decreases as the droplet moves from potential ϕ_J to ϕ_f. The lower bound of the inequality corresponds to the case where all the charge is evaporated at the breakup, while the upper bound corresponds to the limit in which all charge evaporates at potential ϕ_f. Furthermore, using the potential drop along the cone jet $\Delta\phi_J = \phi_E - \phi_J$, and neglecting the dissipation taking place in the cone jet compared to the gain in kinetic energy, $\frac{1}{2}\zeta_J v_J^2 \cong \Delta\phi_J$, Eq. (19a) is recast in the form

$$\phi_{\mathrm{RP}} = \phi_J - \phi_{EV} + \frac{\zeta_f}{\zeta_J}\Delta\phi_J + \zeta_f \int_{\phi_f}^{\phi_J} \frac{d\phi}{\zeta} = \phi_J + \frac{\zeta_f}{\zeta_J}\Delta\phi_J + \mathcal{C}, \tag{19b}$$

$$\text{with} \quad 0 < \mathcal{C} < \left(\frac{\zeta_f}{\zeta_0} - 1\right)\Delta\phi_{EV}.$$

The sum of the first two terms in (19b) is the retarding potential of a primary droplet with mass-to-charge ratio ζ_f. This value is increased by the evaporation of charge in the amount $\mathcal{C}$, which is maximum when the ions evaporate downstream of the extractor, in the long section preceding the electrostatic mirror at ground potential. In this case, and using the 230-nA beam at 21 °C, $\Delta\phi_{EV} = \phi_J = 1495$ V and only $\zeta_f/\zeta_0 = 1.13$ is needed to make the retarding potential of these charged-depleted droplets equal to the potential of the emitter. A larger ζ_f/ζ_0 ratio is necessary if the evaporation occurs along the much shorter fly path between the jet breakup and the extractor. We cannot think of an alternative mechanism that can augment the retarding potential of these low-ζ droplets in excess of the potential of the emitter, sometimes by as much as 200 V. Finally, we note that the low-energy tail of the ion peak P_1 is a strong indication of ion emission from droplets in flight. For example, P_1 in Fig. 4 displays a slow decay between 1500 V $\lesssim \phi_{\mathrm{RP}} \lesssim$ 1000 V, which possibly extends down to about 500 V. Since the retarding potential of these ions is the potential

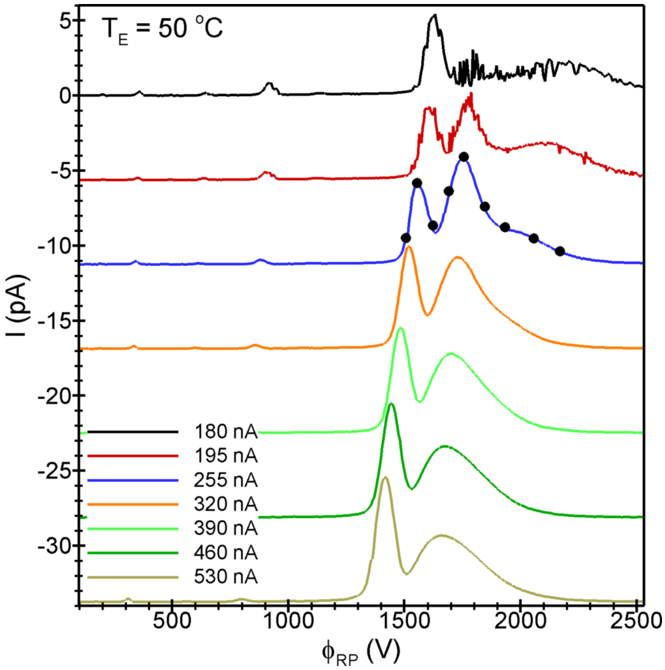

FIG. 11. Retarding potential curves for several beam currents at 50 °C.

from which they are emitted, the ions in the low-energy tail of P_1 are emitted several hundred volts downstream of the jet breakup ($\phi_J = 1560$ V, estimated as the retarding potential of the maximum of P_1). This is consistent with ion emission from droplets in flight between the breakup and the extractor.

When ion field evaporation from droplets becomes more intense, either because the critical droplet is smaller and more charged or its temperature is higher, the ion emission constraint (18) has a smaller slope and intersects the equipotential diameter and Rayleigh limit curves at higher values of ζ_D/ζ_J. Under such conditions, only the droplets with the highest mass-to-charge ratios remain unchanged during flight, while most others evaporate a large fraction of their charge and Coulomb explosions may be suppressed. The EMI-Im beams at 50 °C exhibit this behavior. At constant beam current increasing the temperature of the fluid promotes ion evaporation because the electrical conductivity increases significantly with temperature, increasing the electric field normal to the surface of the cone jet; the larger temperature increases the number of ions than can overcome the energy barrier impeding emission. Figure 11 shows retarding potential curves for several beam currents at 50 °C. At the largest beam currents the curves are similar to those measured at 21 °C, except for the higher current values of all ionic peaks relative to the maximum of the droplet distribution. Starting at 320 nA and increasing at lower beam current, the region $\phi_{RP} \gtrsim 1850$ V separates from the central droplet zone, forming a separate population at the lowest beam current. Furthermore, the area of the central droplet region (this is where the primary droplets preferentially appear) becomes smaller compared to the area of the new droplet population, almost disappearing at the lowest stable beam current of 180 nA. Although retarding potential analysis does not yield the mass-to-charge ratio distributions, it is apparent from the previous discussion that the increasingly dominating droplet population at $\phi_{RP} \gtrsim 1850$ V is formed by droplets that have lost charge by ion emission, and that most droplets become ion emitters at the lowest beam currents. Figure 12 shows TOF spectra for the 255-nA beam (measured at the retarding potentials indicated by black dots in Fig. 11), together with a chart with the average mass-to-charge ratios and standard

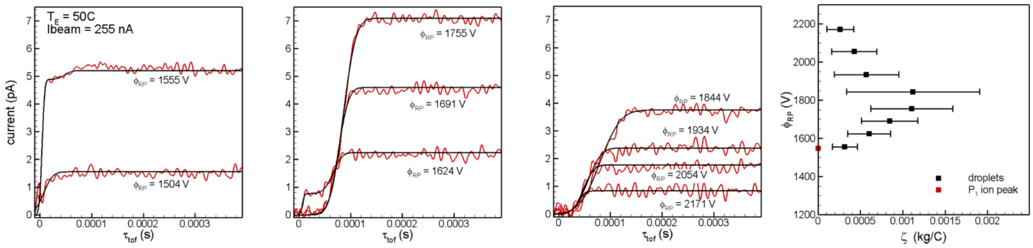

FIG. 12. TOF spectra for a 255-nA beam at 50 °C, and average mass-to-charge ratios and standard deviations of the droplet populations.

deviations of the droplet populations. The phenomenology up to the maximum of the droplet region, $\phi_{\mathrm{RP}} = 1755$ V, is similar to that described at 21 °C, with only ions appearing under most of the P_1 peak, and a combination of ions and droplets in the overlap region followed by a single family of droplets up to $\phi_{\mathrm{RP}} = 1755$ V. At larger retarding potential the phenomenology changes: the average charge-to-mass ratio of the droplets decreases, reaching a minimum value for all droplet populations at the highest retarding potential 2171 V. These droplets must have evaporated a fraction of their charge. Note also the very broad distribution at the turning point $\phi_{\mathrm{RP}} = 1844$ V, likely indicating a coexistence of the two types of droplets (primary droplets and ion evaporating droplets). As the retarding potential increases, the standard deviations decrease, probably reflecting a reduction of primary droplets and a constraining of the ion-emitting droplets: only those with the smallest mass-to-charge ratios, and therefore the smallest radii and largest electric fields, can evaporate a fraction of their charge large enough to sufficiently increase their retarding potentials.

V. CONCLUSIONS

Electrosprays of highly conducting liquids ($K \gtrsim 0.5$) produce beams of charged nanodroplets and molecular ions. The natural breakup of its jet, Coulomb explosions, ion field evaporation, and spontaneous desolvation of molecular ions shape the distributions of particles in the beam. Retarding potential and time-of-flight analysis in tandem provides a wealth of experimental information, including the velocity and electric potential of the jet in the breakup region [23,24]. The radius of the jet, derived from the computed velocity, remains nearly independent of the flow rate when normalized with Gañán-Calvo's characteristic length [5]. This is a well-known property of the much smaller transition region between cone and jet [14,26], and its extension far downstream suggests that the breakup may be triggered by the local behavior of the transition region. Experimental values of the velocity and electric potential at a point of the jet are ideal validation parameters for numerical models of the cone jet, and much needed due to the difficult probing of this nanometric system. The velocity and electric potential in the breakup are also key initial conditions for any model of the expansion of electrospray beams [24].

Due to the much smaller electric relaxation time compared to flow times, the jet breakup of highly conducting liquids is nearly equipotential. When combined with the very high values of the Taylor number Ψ, and less importantly with the high Ohnesorge number ($\mathrm{Oh} = J^{-1/2}$) of highly electrified and viscous nanojets, the breakup produces critical droplets significantly smaller than the value $R_D^*/R_J = 1.89$ typical of inviscid jets without electrification [23]. Furthermore, the critical radius $R_D^*(J, \Psi)$ is at, or slightly above, the Rayleigh stability limit for a droplet with the mass-to-charge ratio of the jet ζ_J. Since the randomness of the breakup produces droplets with radii and mass-to-charge ratios other than R_D^* and ζ_J, and the equipotential breakup distributes these values near $R_D \propto \zeta_D^{1/2}$, most droplets with mass-to-charge ratios larger than ζ_J have radii smaller than their Rayleigh limit, are stable, and remain intact during flight. The $\{\zeta, \phi_{\mathrm{RP}}\}$ values of these primary droplets make it possible to obtain the velocity and potential of the jet. On the other hand, most droplets with mass-to-charge ratios smaller than ζ_J are unstable and undergo Coulomb explosions to produce fragments with smaller mass-to-charge ratios. These fragments appear in the experiments as droplets with low mass-to-charge ratio that do not conform to the breakup condition (6). Furthermore, the smallest droplets with the lowest mass-to-charge ratios have electric fields exceeding the value triggering significant ion emission, and shed charge at constant radius. These droplets form a distinct population with the lowest mass-to-charge ratios and highest retarding potentials (significantly in excess of the emitter potential) in the beam.

Ions carry an important fraction of the beam current. The ion fraction is a weak function of the flow rate and increases with temperature, in qualitative agreement with both the scaling of the electric field normal to the surface of the cone jet and the field emission equation [14,21]. The analysis of the retarding potential curves shows the existence of EMI$^+$ ions joined to up to four EMI-Im molecules. The retarding potential distribution shows a concentration of ion emission from the breakup region, followed by emission from droplets in flight. Some of these solvated ions lose one or two EMI-Im molecules in flight [25], giving rise to additional isolated peaks in the retarding potential curve.

Although this article describes the phenomenology for the ionic liquid EMI-Im, the findings can be extended to other highly conducting liquids on the bases of the dimensionless numbers $\tilde{Q}$, $\mathrm{Re_K}$, and ε that parametrize the state of the cone jet, and the ion solvation energies regulating the emission of ions from the liquid matrix. The following generalizations for electrosprays of highly conducting ionic liquids emerge: (a) the $\mathrm{Re_K}$ numbers of these liquids are always much smaller than one due to their high viscosities and conductivities; (b) due to the dependence of the minimum dimensionless flow rate on $\mathrm{Re_K}$ [28], these liquids operate at $\tilde{Q} \gg 1$; (c) the breakup is invariably nearly equipotential due to the high values of $\tilde{Q}$ and low value of $\mathrm{Re_K}$; (d) the Taylor numbers are near one or larger than one due to the high values of $\tilde{Q}$; (e) because of the large Taylor number, small-J parameter, and the equipotential breakup, the critical droplet radius normalized with the jet radius follows the small-J limit shown in Fig. 9. Accordingly, the jet breakup phenomenology of highly conducting ionic liquids will be similar to that of EMI-Im, with the possible exception of ion emission effects which also depend on the solvation energies specific to the ion-liquid matrix pair. In the case of highly conducting liquids of reduced viscosity, which may be able to operate at significantly lower dimensionless flow rates, the jet breakup phenomenology may be different due to the lower jet electrification and a departure from the equipotential breakup limit.

ACKNOWLEDGMENTS

This research was supported by NASA's Space Technology Research Early Stage Innovations program, Grant No. NNX17AD01G, and by Jet Propulsion Lab's Award No. 1620723.

---

[1] M. Cloupeau and B. Prunet-Foch, Electrostatic spraying of liquids in cone-jet mode, J. Electrost. **22**, 135 (1989).

[2] M. Cloupeau and B. Prunet-Foch, Electrostatic spraying of liquids. Main functioning modes, J. Electrost. **25**, 165 (1990).

[3] J. Fernández de la Mora and I. Loscertales, The current emitted by highly conducting Taylor cones, J. Fluid Mech. **260**, 155 (1994).

[4] J. Rosell-Llompart and J. Fernández de la Mora, Generation of monodisperse droplets 0.3 to 4 μm in diameter from electrified cone-jets of highly conducting and viscous liquids, J. Aerosol Sci. **25**, 1093 (1994).

[5] A. M. Gañán-Calvo, Cone-Jet Analytical Extension of Taylor's Electrostatic Solution and the Asymptotic Universal Scaling Laws in Electrospraying, Phys. Rev. Lett. **79**, 217 (1997).

[6] F. Higuera, Flow rate and electric current emitted by a Taylor cone, J. Fluid Mech. **484**, 303 (2003).

[7] J. Fernández de la Mora, The fluid dynamics of taylor cones, Annu. Rev. Fluid Mech. **39**, 217 (2007).

[8] A. Gañán-Calvo, J. López-Herrera, M. Herrada, A. Ramos, and J. Montanero, Review on the physics of electrospray: From electrokinetics to the operating conditions of single and coaxial Taylor cone-jets, and AC electrospray, J. Aerosol Sci. **125**, 32 (2018).

[9] J. Rosell-Llompart, J. Grifoll, and I. Loscertales, Electrosprays in the cone-jet mode: From Taylor cone formation to spray development, J. Aerosol Sci. **125**, 2 (2018).

[10] M. Gamero-Castaño and J. Fernández de la Mora, Direct measurement of ion evaporation kinetics from electrified liquid surfaces, J. Chem. Phys. **113**, 815 (2000).

[11] M. Gamero-Castaño, Electric-Field-Induced Ion Evaporation from Dielectric Liquid, Phys. Rev. Lett. **89**, 147602 (2002).

[12] M. Gamero-Castaño, Dissipation in cone-jet electrosprays and departure from isothermal operation, Phys. Rev. E **99**, 061101(R) (2019).

[13] M. A. Herrada, J. M. López-Herrera, A. M. Gañán-Calvo, E. J. Vega, J. M. Montanero, and S. Popinet, Numerical simulation of electrospray in the cone-jet mode, Phys. Rev. E **86**, 026305 (2012).

[14] M. Gamero-Castaño and M. Magnani, Numerical simulation of electrospraying in the cone-jet mode, J. Fluid Mech. **859**, 247 (2019).

[15] A. McEwen, H. Ngo, K. LeCompte, and J. Goldman, Electrochemical properties of imidazolium salt electrolytes for electrochemical capacitor applications, J. Electrochem. Soc. **146**, 1687 (1999).

[16] E. Grustán-Gutierrez and M. Gamero-Castaño, Microfabricated Electrospray Thruster Array with High Hydraulic Resistance Channels, J. Propul. Power **33**, 984 (2017).

[17] M. Gamero-Castaño, Characterization of the electrosprays of 1-ethyl-3-methylimidazolium bis(trifluoromethylsulfonyl) imide in vacuum, Phys. Fluids **20**, 032103 (2008).

[18] M. Gamero-Castaño and V. Hruby, Electrospray as a source of nanoparticles for efficient colloid thrusters, J. Propul. Power **17**, 977 (2001).

[19] M. Gamero-Castaño, Retarding potential and induction charge detectors in tandem for measuring the charge and mass of nanodroplets, Rev. Sci. Instrum. **80**, 053301 (2009).

[20] C. Daguenet, P. J. Dyson, I. Krossing, A. Oleinikova, J. Slattery, C. Wakai, and H. Weingaertner, Dielectric response of imidazolium-based room-temperature ionic liquids, J. Phys. Chem. B **110**, 12682 (2006).

[21] J. V. Iribarne and B. A. Thomson, On the evaporation of small ions from charged droplets, J. Chem. Phys. **64**, 2287 (1976).

[22] A. Gañán-Calvo, On the general scaling theory for electrospraying, J. Fluid Mech. **507**, 203 (2004).

[23] M. Gamero-Castaño and V. Hruby, Electric measurements of charged sprays emitted by cone-jets, J. Fluid Mech. **459**, 245 (2002).

[24] M. Gamero-Castaño, The structure of electrospray beams in vacuum, J. Fluid Mech. **604**, 339 (2008).

[25] C. E. Miller and P. C. Lozano, Measurement of the dissociation rates of ion clusters in ionic liquid ion sources, Appl. Phys. Lett. **116**, 254101 (2020).

[26] M. Gamero-Castaño, Energy dissipation in electrosprays and the geometric scaling of the transition region of cone-jets, J. Fluid Mech. **662**, 493 (2010).

[27] J. Fernández de la Mora, On the outcome of the coulombic fission of a charged isolated drop, J. Colloid Interface Sci. **178**, 209 (1996).

[28] M. Gamero-Castaño and M. Magnani, The minimum flow rate of electrosprays in the cone-jet mode, J. Fluid Mech. **876**, 553 (2019).

[29] A. Gañán-Calvo, J. Dávila, and A. Barrero, Current and droplet size in the electrospraying of liquids. Scaling laws, J. Aerosol Sci. **28**, 249 (1997).

[30] S. Chandrasekhar, *Hydrodynamic and Hydromagnetic Stability*, Dover Books on Physics Series (Dover, New York, 1981).